Supporting the detection and monitoring of volcanic clouds: A promising new application of Global Navigation Satellite System radio occultation

Riccardo Biondi [a,b], Andrea K. Steiner [a,c,*], Gottfried Kirchengast [a,c], Hugues Brenot [d], Therese Rieckh [a,e]

[a] Wegener Center for Climate and Global Change (WEGC), University of Graz, Graz, Austria
[b] Beneficiary of an AXA Research Fund Postdoctoral Grant, Institute for Atmospheric Sciences and Climate (ISAC-CNR), Rome, Italy
[c] Institute for Geophysics, Astrophysics, and Meteorology/Institute of Physics, University of Graz, Graz, Austria
[d] Belgian Institute for Space Aeronomy (BIRA-IASB), Brussels, Belgium
[e] COSMIC Program, University Corporation of Atmospheric Research (UCAR), Boulder, CO, USA

Abstract

The altitude of volcanic clouds and the atmospheric thermal structure after volcanic eruptions are studied using Global Navigation Satellite System (GNSS) Radio Occultation (RO) profiles co-located with independent radiometer images of ash and sulfur dioxide plumes. We use geographically co-located RO profiles to detect the top altitude of volcanic clouds and to analyze their impact in terms of temperature change signatures. We obtained about 1300 RO profiles co-located with two representative eruptions (Puyehue 2011, Nabro 2011) and found that an anomaly technique recently developed for detecting convective cloud tops and studying the vertical thermal structure of deep convective systems can also be applied to volcanic clouds. Analyzing the atmospheric thermal structure after the eruptions, we found clear cooling signatures induced by volcanic cloud tops in the upper troposphere for the Puyehue case. For the Nabro case we detected a significant warming in the stratosphere which lasted for several months, indicating that the cloud reached the stratosphere. The results are encouraging for future large-scale use of RO data for supporting the monitoring of volcanic clouds and their impacts on weather and climate.

1. Introduction

Explosive volcanic eruptions produce large ash clouds and inject huge amounts of gas, aerosol, and ash into the troposphere, which can even reach into the stratosphere (Sparks et al., 1997; Bourassa et al., 2012, 2013; Fromm et al., 2013, 2014). Major volcanic eruptions can cause short-term climate change (Robock, 2000) if sulfur dioxide

(SO_2) is injected into the stratosphere, forming sulfate aerosols with a long residence time (about 1–3 years). The effect is a warming of the stratosphere, by aerosols and also induced circulation, and a cooling of the troposphere as was observed for the Mount Pinatubo eruption in 1991 (McCormick et al., 1995; Robock, 2000). The impacts largely depend on the total mass erupted, the altitude reached by the ash and SO_2, the location of the volcano, and the extent of the dispersion due to atmospheric circulation. Under certain atmospheric conditions volcanic

ash clouds can spread over thousands of kilometers in just a few hours (Textor et al., 2005).

Ash clouds are a threat for aviation transport (Prata, 2008), since they can damage the aircraft engines even at large distances from the eruption. In 2010, the Eyjafjallajökull eruption in Iceland (Stohl et al., 2011) generated the largest air traffic shutdown since the Second World War with an estimated loss of about 3 billion U.S. dollars for the airline industry and with major effects on social and economic activities.

Research attention has focused on the improvement of detection and monitoring of volcanic ash clouds, which had already been advocated by Tupper et al. (2004). The ESA-EUMETSAT workshop on "Monitoring volcanic ash from space" (Zehner, 2010) provided a list of recommendations stating that "*Studies should be made of potential new satellites and instruments dedicated to monitoring volcanic ash plumes and eruptions*" and highlighting the difficulty of monitoring such events with the current knowledge.

Observing the density of the ash cloud as function of height is one of the major challenges (Mackie et al., 2016), since values larger than 2 mg/m^3 are considered dangerous for aircraft engines, according to recommendations derived from the experience with the Eyjafjallajökull eruption (IFALPA, 2011). This parameter could only be detected by flying into the cloud with all related risks just until recently when infrared spectral imaging showed promising results (Prata et al., 2016). The mass flux of the eruption is fundamentally related to the maximum height reached by a volcanic plume (Woods, 1988). This volcanic cloud top altitude can be detected with different techniques (ground based, *in situ*, satellite), but typically with quite low accuracy.

Knowledge of the cloud top altitude is essential, however, to provide information on ash-free altitude regions for air traffic and on potential overshooting and spread of SO$_2$ into the stratosphere, which impacts climate. The discrimination of ash clouds from other types of clouds is challenging, wherefore Tupper et al. (2004) state "*a reliable detection system cannot be dependent on the meteorological conditions and it is necessary to have a weather independent warning capacity*". Along these lines the potential of the relatively new satellite technique of radio occultation (RO) based on Global Positioning System (GPS) signals, or more generally Global Navigation Satellite System (GNSS) signals, comes into play (Biondi et al., 2012, 2013).

In this study we provide an assessment of the potential capacity of the RO technique for supporting volcanic cloud detection and monitoring. Preliminary results on this work have been reported in a discussion paper by Biondi et al. (2016) and, for completeness and clarity of introduction, the introductory Sections 1 and 2 of this study are similar to the introductory part of that discussion paper. The present study provides substantiated initial results on the capacity of RO to support volcanic cloud monitoring, highlighting this capacity as a promising new GNSS application in meteorology and climate. Section 2 provides an overview of the available observing techniques and introduces the potentially unique role of RO data. Section 3 then summarizes the data sets used and Section 4 describes the study cases (two example eruptions) and methods. Subsequently we discuss the results in Section 5 and draw conclusions in Section 6.

2. Volcanic cloud observing techniques

Volcanic ash clouds are currently monitored by the International Airways Volcano Watch using a combination of ground-based sensors, satellite sensors, and aircraft measurements, but each of these methods has some temporal, spatial or technological limitation. According to the International Union of Geodesy and Geophysics (IUGG) only about 50% of the world's volcanoes that currently threaten air operations have any sort of ground-based monitoring (IUGG, 2010). The greatest danger for air traffic is the time just after the eruption when no warnings are available, models are not reliable, and atmospheric observations are sporadic. The vertical resolution of most satellite data is very coarse for monitoring such phenomena and thus there is an urgent need to gather information on the vertical structure of evolving volcanic clouds (Zehner, 2010).

Geostationary satellite data (e.g., the Spinning Enhanced Visible and InfraRed Imager) and polar-orbiting satellite data (e.g., the Advanced Very High Resolution Radiometer, and the Moderate-Resolution Imaging Spectroradiometer - MODIS) are used for detecting and monitoring volcanic clouds (Holasek and Self, 1995; Woods et al., 1995; Prata, 2008; Clarisse et al., 2012; Theys et al., 2013), but they cannot profile the atmosphere vertically and measurements are affected by the presence of other types of clouds. Research aircraft are very useful for getting information about the ash extent and concentration. They provide accurate products, but they are not operational, the spatial coverage is limited, and technical limitations are the same as for commercial aircraft, i.e., they cannot fly where the ash concentration is too high. Ground-based instruments such as lidars (Sawamura et al., 2012), radars (Harris and Rose, 1983; Sawada, 2004), and cameras are also important for monitoring the eruptions, but they are too sparse and with limited spatial coverage.

Many techniques have been developed for detecting clouds and their top heights (Frey et al., 1999; Dubiusson et al., 2009; Chang et al., 2010; Stohl et al., 2011; Poulsen et al., 2012), including ash clouds (Prata, 2008; Clarisse et al., 2012) and SO$_2$ clouds (Prata, 2008; Theys et al., 2013), relying on different satellite measurements with different resolutions such as the Global Ozone Monitoring Experiment, the Ozone Monitoring Instrument (OMI), the Infrared Atmospheric Sounding Interferometer (IASI), MODIS, and the Atmospheric InfraRed Sounder (AIRS). The Cloud-Aerosol Lidar with Orthogonal

Polarization (CALIOP) on board of the Cloud-Aerosol Lidar and Infrared Pathfinder Satellite Observations (CALIPSO) satellite is able to profile the volcanic ash cloud with very high vertical resolution (Vernier et al., 2013a), but the temporal resolution is not adequate for following the development of the plume and sometimes the discrimination of ash plumes from other type of clouds is problematic.

The GNSS RO technique is highly complementary to these other systems, enabling measurement of atmospheric density and temperature structure in nearly all meteorological weather conditions, during day and night, and with high vertical resolution and high accuracy (e.g., Anthes, 2011; Steiner et al., 2011). Several GNSS RO missions are operating at present, providing vertical atmospheric profiles with good global coverage in space and time, like the US/Taiwan FORMOSAT-3/COSMIC six-satellite constellation (Anthes et al., 2008) or the European Meteorological Operational (MetOp) satellite series (Luntama et al., 2008).

The use of RO data in numerical weather prediction has improved weather forecasting especially in remote and data sparse areas of the globe (e.g., Cardinali, 2009) as well as tropical cyclone track forecasting (e.g., Huang et al., 2005). Moreover, RO can deliver accurate information on the thermal structure and cloud top altitude of convective systems and tropical cyclones as demonstrated recently by Biondi et al. (2012, 2013, 2015). Monthly RO climatologies were recently also used, together with radiosonde and reanalysis data, in a study aiming to detect temperature effects of minor volcanic eruptions over 2001–2010 (Mehta et al., 2015). Due to its characteristics, RO is a potentially valuable technique to study the structure of volcanic clouds and to complement current monitoring systems. In this study we investigate whether the anomaly technique developed by Biondi et al. (2013, 2015) can be applied as well for monitoring volcanic clouds, in particular for determining their cloud top height, their thermal structure and influence on short-term climate.

3. Data sets used

3.1. GNSS radio occultation data

GNSS RO is an active limb sounding method using a satellite-to-satellite link. GNSS satellites transmit radio signals which are influenced by the Earth's refractivity field along their propagation path to a receiver on a Low Earth Orbit (LEO) satellite. Movement of the satellites leads to vertical scanning of the entire troposphere and stratosphere within about one minute and provides measurements with high vertical resolution but inherent along-ray horizontal averaging. The horizontal resolution across-ray is about 1.5 km and the along-ray resolution ranges from about 60 km in the lower troposphere to about 300 km in the stratosphere (Melbourne et al., 1994; Kursinski et al., 1997). The vertical resolution ranges from near 100 m in

the lower troposphere to about 1 km in the stratosphere (Gorbunov et al., 2004). The quality of RO measurements is best in the upper troposphere and lower stratosphere (UTLS) with an accuracy of 0.7 K to 1 K between 8 km and 25 km for individual temperature profiles (Scherllin-Pirscher et al., 2011a, 2017).

Data from the following RO missions were used: CHAllenging Minisatellite Payload (CHAMP) (Wickert et al., 2001), Satélite de Aplicaciones Científicas (SAC-C) (Hajj et al., 2004), Gravity Recovery And Climate Experiment (GRACE-A) (Beyerle et al., 2005; Wickert et al., 2009), and FORMOSAT-3/COSMIC (Anthes et al., 2008), altogether comprising about 2000 globally distributed RO profiling measurements per day. RO data from different missions are highly consistent and agree within 0.2 K between 4 km and 35 km for temperature (Scherllin-Pirscher et al., 2011a), which allows merging of the data without inter-calibration or homogenization (Foelsche et al., 2011; Steiner et al., 2011). Available RO data products include individual profiles as well as gridded climatologies (e.g., Ho et al., 2012; Steiner et al., 2013).

For this study we used RO bending angle and temperature profiles, processed by the Wegener Center for Climate and Global Change (WEGC) with the Occultation Processing System (OPS) version 5.6 (Schwärz et al., 2016), based on excess phase and orbit data version 2010.2640 from the University Corporation for Atmospheric Research (UCAR). In the OPS processing, bending angle is initialized at high altitudes with background data from the European Centre for Medium-Range Weather Forecasts (ECMWF) short-range forecasts. Below 30 km, the retrieved bending angle profiles only contain observational information from RO. Temperature profiles in the stratosphere, where water vapor influence is negligible, are directly retrieved from the RO data while temperature profiles in the troposphere with its significantly higher moisture content are retrieved based on optimal estimation of RO and ECMWF short-range forecast profiles. The latter auxiliary data from ECMWF contribute relevant information in the lower to middle troposphere only.

A detailed description of the OPS retrieval is given by Schwärz et al. (2016; Appendix A therein) and error estimates for all retrieved variables from bending angle to temperature are given by Scherllin-Pirscher et al. (2011a, 2011b, 2017). Scherllin-Pirscher et al. (2011b) also explain and illustrate the difference between retrievals of RO dry-air atmospheric profiles and moist-air tropospheric profiles. The observational uncertainty of individual temperature profiles is about 0.7 K in the tropopause region and slightly decreases toward the lower troposphere as shown by Scherllin-Pirscher et al. (2017). RO atmospheric profiles have been excessively validated and compared with a range of independent observations, including radiosondes and satellite limb sounder data (e.g., Ladstädter et al., 2015; Schwärz et al., 2016), showing the high quality of RO profiles in the UTLS.

Bending angle profiles provide information about the refraction of the GNSS radio signals in the atmosphere due to the (mainly vertical) variations in the atmospheric refractivity, which in turn depends on pressure, temperature, and water vapor pressure (Smith and Weintraub, 1953; Kursinski et al., 1997). Bending angle thus intrinsically contains information on vertical variations due to pressure, temperature, and water vapor changes. At the UTLS altitudes of interest to this study, water vapor effects are very small to negligible as noted above, and refractivity is proportional to air density, i.e., to the ratio of pressure and temperature. Therefore bending angle variations are dominated by temperature variations. However, the bending angle profile is complementary to the temperature profile and it is the more directly observed RO profile. Temperature is obtained later in the RO processing chain, after refractivity retrieval and vertical pressure integration, so that it is somewhat more smoothed. We therefore employ both variables, bending angle with its finer resolution of vertical structure also as the key variable for cloud top detection, and temperature for the direct characterization of anomalies in the atmospheric thermal structure.

Reference climatologies for bending angle and temperature were obtained by averaging all RO profiles collected in the period 2001 to 2012 to monthly means on a $1° \times 1°$ grid in latitude and longitude, using a resolution of $5° \times 5°$ around each grid point (i.e., grid cell size of about 500 km extension). This leads to about 100–400 RO profiles averaged per grid cell (the specific number depending on month and latitude) and ensures a robust average that is representative of large-scale background field resolution. Vertically, the climatology is set up at a sampling grid of 100 m covering the full troposphere and stratosphere. Constructed this way, the reference climatology is available with global coverage on a $1° \times 1° \times 100$ m (latitude $\times$ longitude $\times$ altitude) sampling grid, for both bending angle and temperature. It can be used to extract a collocated long-term mean climatological profile at any desired RO event location, where the extracted profile can then serve as reference to compute an anomaly profile (see Section 4.2).

3.2. AIRS and OMI data

We used ash observations from AIRS and SO_2 observations from OMI to geographically identify the area covered by volcanic clouds and to differentiate between volcanic ash clouds and SO_2 clouds (see Section 4.1). AIRS is a thermal infrared (IR) sensor (Aumann et al., 2003) on-board the Aqua satellite. OMI is an ultraviolet-visible (UV-Vis) spectrometer (Levelt et al., 2006) onboard Aura. Both these polar orbiting satellite radiometers operate in nadir mode, with footprints of 15 km in diameter and of 13 km $\times$ 24 km, respectively, corresponding to the horizontal resolution of the resulting images.

AIRS measures the spectrum of the thermal radiation emitted by the Earth-atmosphere system (at wavelengths from 0.4 μm to 1.0 μm and from 3.7 μm to 15.4 μm, during day and night). OMI measures the solar irradiance spectrum (i.e., light backscattered by the atmosphere or reflected by the Earth during daytime) at wavelengths from 270 nm to 400 nm, where SO_2 has strong and distinctive absorption bands. The OMI SO_2 retrieval (Yang et al., 2007) provides integrated SO_2 concentrations expressed in Dobson Units (1 DU = 2.69×10^{16} molecules/cm^2).

A selective detection of ash from AIRS is employed for the ash cloud images used in this study, based on a robust volcanic ash detection method (Clarisse et al., 2013) differentiating ash from normal water clouds, sand and other dust. The resulting AIRS ash index comes with three levels of confidence (low, medium, high). A pixel with a high level of confidence indicates that the presence of ash is almost certain. The ash concentration itself is not provided and this very selective ash detection is not effective for low ash concentrations. More details about ash and SO_2 image data products and their limitation are reported by Brenot et al. (2014).

3.3. CALIPSO data

We used level 1 total attenuated backscatter products from CALIOP (CAL_LID_L1, version V3.01). CALIOP is a two wavelength (532 nm/ 1064 nm) lidar onboard the CALIPSO satellite with a vertical resolution of 30 m/60 m and a horizontal resolution of 330 m/1000 m, respectively, in the UTLS up to 20 km altitude (Winker et al., 2009). CALIOP attenuated backscatter data were used for detecting the ash cloud altitude with high accuracy. The altitude where the attenuated backscatter at 532 nm is, from top downward, starting to be larger than the background noise is determined to be the cloud top altitude.

3.4. MODIS data

MODIS is an imaging spectroradiometer flying aboard the Terra and Aqua spacecraft. The wide spectral range of MODIS allows monitoring physical and optical cloud properties with global coverage (King et al., 2013). We used NASA MODIS Atmosphere Images Hi-Res Global Mosaic cloud data for defining clear air conditions and conditions with deep convection by using the cloud top pressure (MYD06_L2 and MOD06_L2) as reference (http://modis-atmos.gsfc.nasa.gov/index.html).

4. Study cases and methods

4.1. Volcanic eruption events

We have analyzed two eruptions with different characteristics as respective study cases illustrated in Fig. 1: the Puyehue eruption in June 2011, which was mainly an ash eruption, and the Nabro eruption in June 2011, which was mainly an SO_2 eruption.
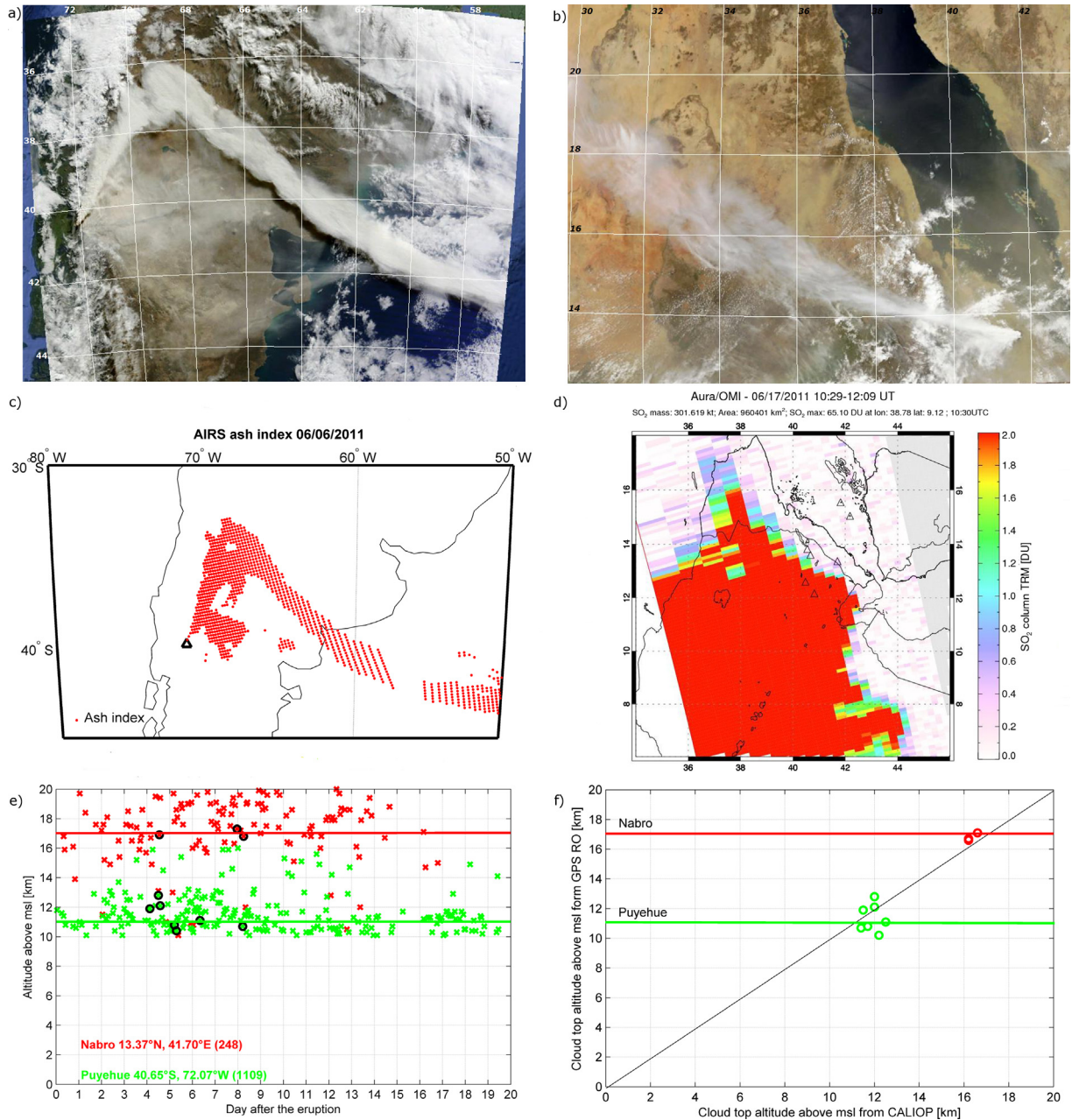
Fig. 1. (a) Terra MODIS natural-color image of the Puyehue volcanic plume on June 6, 2011 (Credit: Jeff Schmaltz, MODIS Rapid Response Team, NASA GSFC; http://earthobservatory.nasa.gov/NaturalHazards/view.php?id=50858). (b) Aqua MODIS natural-color image of the Nabro volcanic plume on June 13, 2011 (Credit: same as (a), but with image id = 50988). (c) Puyehue ash plume on June 6, 2011 from AIRS data showing the (high confidence level) ash index (Clarisse et al., 2013). (d) Nabro SO$_2$ plume on June 17, 2011 from Aura OMI data (Credit: MEaSUREs Project, NASA GSFC; https://so2.gsfc.nasa.gov/pix/daily/0611/afar_0611z.html). (e) Cloud top altitudes of volcanic plumes (cross symbols) for Puyehue (green) and Nabro (red), derived from RO data over the first 20 days from the eruption; co-located CALIOP data are indicated (black circles). Numbers in brackets denote the number of RO profiles. (f) Consistency between cloud top altitudes derived from RO with the closest cloud top altitudes from CALIOP (circles). Horizontal solid lines denote the respective monthly climatological tropopause altitudes for the two volcano locations. (For interpretation of the references to color in this figure legend, the reader is referred to the web version of this article.)

The Puyehue volcano in Chile (40.35 °S, 72.07 °W) erupted on 4 June 2011 until 6 June 2011 (Fig. 1a), followed by a minor eruption on 12 to 14 June 2011 and high alert levels persisting through early 2012 (Global Volcanism Program, 2013). The eruption on 4 June 2011 produced a set of plumes including an ash plume with its top near 12 km altitude. This eruption affected the South-

ern Hemisphere with its ash cloud (Fig. 1c) spreading about 60 degrees in latitude and 360 degrees in longitude and finishing its first circle around the globe on 18 June 2011. Several flights in the Southern Hemisphere were cancelled due to the ash in the atmosphere.

During the night of 12 to 13 June 2011 an explosive eruption occurred at the Nabro volcano located in Eritrea

(13.37 °N, 41.70 °E) as shown in Fig. 1b. The Nabro eruption has been recognized as the largest stratospheric sulfur injection since Pinatubo in 1991 (Timmreck et al., 2013; Bourassa et al., 2012; Robock, 2013), injecting mainly SO_2 into the atmosphere (Fig. 1d), which spread more than 60 degrees in latitude and more than 100 degrees in longitude within a few days. Nabro eruptions occurred from the initial eruption in June until mid-July 2011 and thermal alerts were recorded until June 2012 (Global Volcanism Program, 2014).

The initial plume of Nabro was found to be rich in water vapor and sulfur dioxide, located between 15 km and 17 km. It underwent uplift within the Asian Monsoon circulation up to the tropopause near 17 km and ascended further into the stratosphere. Large stratospheric plumes were observed up to 21 km after the eruption. The resulting sulfate cloud was heating the upper troposphere and the lower stratosphere due to absorption in the infrared. At stratospheric heights, a major atmospheric sink for SO_2 is oxidation, leading to the formation of hydrated sulfuric acid droplets, i.e., to a sulfate aerosol cloud (Clarisse et al., 2014). If water vapor is present, sulfate aerosols form faster due to the abundance of hydroxyl radicals which accelerate SO_2 oxidation. The implication is a faster stratospheric aerosol optical depth (SAOD) formation during the first few months after a water vapor rich eruption, also leading to a higher SAOD overall (LeGrande et al., 2016). Approximately 60% of the SAOD that followed the Nabro eruption was attributable to the lower stratosphere above about 15 km (Andersson et al., 2015).

4.2. Methods

For the selected eruption cases (Puyehue and Nabro), we located in a first step the ash and SO_2 plumes, using the AIRS ash index data for Puyehue (considering high level of confidence only) and the OMI SO_2 data for Nabro, respectively, as illustrated in Fig. 1c and d. Spreading about 1000 km in one day (Textor et al., 2005; Bignami et al., 2014), the extent of the volcanic cloud well covers the scale of the GNSS RO horizontal resolution (about 200–300 km at the cloud altitudes) and atmospheric signals are large enough to be detected by RO observations.

In a second step, we screened all RO profiles at mean tangent point locations and selected those located within the region of the volcanic plume as defined from AIRS and OMI data for each day after the eruption. Over a time period of 20 days from the eruption we found a total of 1109 profiles co-located with the Puyehue plume, and 248 profiles co-located with the Nabro plume, respectively.

We further selected profiles in basic geographic areas of size 10° × 10° in latitude and longitude, centered at the volcano location. The cloud-collocated datasets in these areas were used as core RO datasets for exploring potential cloud-induced signatures. We complemented them by RO datasets from the same geographic areas outside clouds and during other time periods, in order to put the anomaly signature results from the cloud-collocated datasets into context.

For detecting the cloud top altitude and for analyzing the cloud-induced thermal structure with RO we applied the anomaly technique developed by Biondi et al. (2013) for anomalous atmospheric profile and cloud top detection of convective (water) cloud systems and cyclones. As long-term mean monthly RO reference climatologies for bending angle and temperature, needed to provide co-located reference profiles for the anomaly construction, we used the global 1° × 1° × 100 m (latitude × longitude × altitude) climatologies described in Section 3.1 above.

We computed the bending angle anomaly by referring each selected individual RO bending angle profile in the volcanic cloud area to the RO reference climatology profile extracted for the same location from the global RO bending angle reference climatology for the same month. That is, we subtracted the co-located RO reference climatology profile from the individual RO bending angle profile and then normalized with respect to the reference climatology profile in order to obtain a fractional (percentage) anomaly profile. The cloud top altitude of volcanic clouds, both ash and SO_2 plumes, is represented as pronounced spike in the vertical bending angle anomaly structure.

The criterion chosen for cloud top detection is a bending angle anomaly deviation larger than 3% within a 2 km altitude range, in line with the experience from previous studies (Biondi et al., 2013, 2015) and as found robust in sensitivity tests. We also computed the corresponding temperature anomaly profiles in the same way (directly using it as a difference profile rather than a fractional profile), in order to assess the impact of the volcanic cloud on the atmospheric thermal structure.

The cloud top altitude detected with RO was validated by using co-located CALIOP cloud top data from attenuated backscatter within a spatial distance of 200 km. Although no CALIOP measurements are available for the first days of the Puyehue and Nabro eruptions, we found three RO-CALIOP co-locations for the Nabro cloud for 28 to 29 June 2011 and seven RO-CALIOP co-locations for the Puyehue cloud for the period 15 to 19 June 2011.

5. Results and discussion

5.1. Detection of cloud tops and thermal anomaly signatures

The results show that in case of both ash and SO_2 volcanic clouds, the applied anomaly technique works well. Fig. 1e presents volcanic cloud top altitudes detected from RO observations for the investigated eruption cases of Puyehue and Nabro. The monthly climatological tropopause in the respective regions is at 10.8 km and 17.1 km altitude, respectively, as computed from RO data (Rieckh et al., 2014). The validity of detection of the cloud top altitudes with RO is confirmed with highly accurate reference data from CALIOP observations in Fig. 1f.

The comparison of cloud top altitudes from RO with co-located CALIOP observations shows good agreement for Nabro and Puyehue with a correlation coefficient of 0.94 and a root mean square (r.m.s.) error of 930 m. These values also agree with estimates obtained with photogrammetry techniques (e.g., Genkova et al., 2007; Zakšek et al., 2013; Virtanen et al., 2014). Though only 10 RO-CALIOP co-location pairs were available for this comparison, the r.m.s. error is still quite favorable and fully consistent with the findings for tropical cyclones and convective systems (Biondi et al., 2012, 2013, 2015) and reflects the co-location criterion of 200 km and the different vertical resolution of the observation methods. Future larger co-location datasets will allow the refinement of the estimates of this initial study.

In Fig. 2 we show the temperature and bending angle anomaly profiles before (left panels) and after (right panels) the Puyehue and Nabro eruptions as examples of ash and SO_2 plume effects, respectively. The vertical structure of RO temperature anomaly profiles for the Puyehue eruption (Fig. 2b) reveals a prominent cooling of about –2 K by the volcanic cloud at about 11 km, in agreement with the findings of previous studies with meteorological satellite data (Harris et al., 1981; Matson, 1984) and with a small number of RO data (Wang et al., 2009; Okazaki and Heki, 2012). The cooling corresponds with a strong positive anomaly in bending angle (Fig. 2d). However, it is not possible to discriminate between volcanic ash clouds and convective (water) clouds from RO only, since the cloud top cooling is common for all convective processes (Biondi et al., 2012, 2013, 2015). For the Puyehue eruption (ash cloud), we thus detected the cloud top altitude, but we did not find any clear signature of the volcanic ash in the RO profile. For discrimination of the clouds, additional information on ash is therefore needed, as used in this study by invoking AIRS ash index data.

For the Nabro eruption the analysis was more complex because of the emission of significant amounts of SO_2. Also the atmospheric structure was at the same time affected by the presence of a low tropospheric aerosol cloud influencing the mid-tropospheric temperatures. The tropospheric anomaly feature near 6 km altitude in the Nabro case before and after the eruption (Fig. 2 e and f) is a persistent feature from May to September and is due to dust clouds from pre-monsoon dust storm activity (e.g., Pósfai et al., 2012; Alharbi et al., 2013). We validated this middle-troposphere feature in the RO profiles with aerosol cloud top altitude information from CALIOP backscatter data and found the cloud top altitudes consistent for all investigated months (see also Figs. 3, 4 and 6).

RO temperature anomaly profiles (Fig. 2e) and bending angle anomaly profiles (Fig. 2g) just before the eruption (1 June to 11 June 2011) in the area of Nabro ($10° \times 10°$ in latitude and longitude) show a negative temperature anomaly of about 2.5 K at about 17 km, which occurs close to the monthly climatological tropopause level (black dashed line). This negative temperature anomaly is associated with

strong convective activity from 1 June to 11 June 2011 as discussed in Section 5.2.

During the Nabro eruption we detected the cloud top altitude and, furthermore, we also found a clear signature distinguishing the eruption itself as shown in Fig. 2f for temperature and in Fig. 2h for bending angle anomaly profiles co-located with the volcanic plume (in the $10° \times 10°$ area) just after the eruption. A warm anomaly of nearly 4 K above the monthly-mean climatological tropopause appears as the eruption signature. The volcanic cloud tops (bending angle anomaly peaks) correspond in this case to the primary tropopause (pink area) and the tropopause itself corresponds to the secondary tropopause (cyan area). These results show that also in the case of volcanic eruptions, as for tropical cyclones (Biondi et al., 2015) and convective systems (Biondi et al., 2012), a double tropopause feature can be found, where the evidence suggests that the lower level is caused by the cloud top and the higher level represents the actual tropopause, which is presumably pushed up by the buoyancy flux of the eruption.

The estimated Nabro eruption cloud tops are generally located at an altitude below 17 km (Fig. 2f and h, violet dashed line and associated standard deviation corridor), which is below the climatological tropopause of 17.1 km (Fig. 2f and h, black dashed line). The warming in the lower stratosphere appears then after the eruption, indicating that the SO_2 plume directly reached the stratosphere as reported also by Vernier et al. (2013b) and Fromm et al. (2013, 2014) and that its direct radiative effect induced a stratospheric heating.

This is different from the Puyehue case where there was no SO_2 but an ash plume which induced, likely via its association with convective activity, a cooling rather than a warming. The major reason of the negative temperature anomaly probably comes from a perturbation of the meteorological situation induced by the volcanic cloud. According to Raga et al. (2013) "*The volcanic plume influenced the local meteorology resulting in a decrease of the temperature when compared to the average temperature during days with no plume present.*"

More detailed physical investigation and explanation of these signatures is left for future refined study based on larger and more diverse datasets. The basic and key question that we intend to answer with this initial study is whether these volcanic cloud-induced thermal structures are indeed systematically different and distinguishable from normal atmospheric conditions.

5.2. Are the anomaly signatures indeed volcanic cloud-induced?

We next examine the normal climatological background variability for May and June in years without volcanic eruptions. Fig. 3 shows the monthly mean temperature and bending angle anomalies averaged over May 2007–2013 and June 2007–2013 (excluding the month of eruption June 2011), and their estimated inter-annual variability
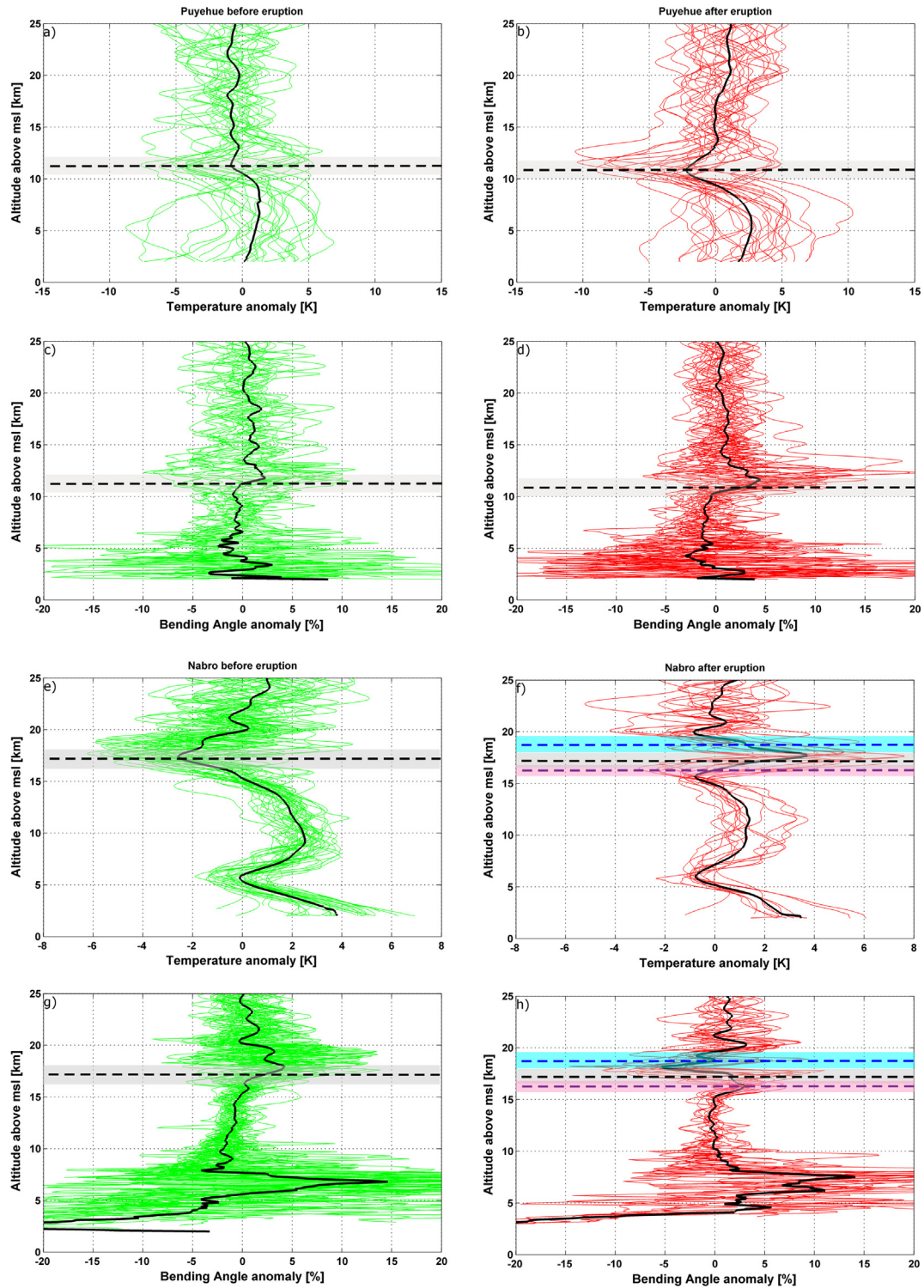
Fig. 2. Puyehue (top four panels) and Nabro (bottom four panels) cases before (left column) and after (right column) the respective eruption (Puyehue starting 5 June 2011, Nabro 12 June 2011). (a and b) Temperature anomaly profiles and (c and d) bending angle anomaly profiles in the area of Puyehue before (green; May 2011, 24 profiles) and after (red; 5–30 June 2011, 26 profiles) the eruption, with the after-eruption profiles co-located with the Puyehue eruptive cloud (AIRS ash index). (e and f) Temperature anomaly profiles and (g and h) bending angle anomaly profiles in the area of Nabro before (green; 1–11 June 2011, 25 profiles) and after (red; 12–20 June 2011, 14 profiles) the eruption, with the after-eruption profiles co-located with the Nabro eruptive cloud (OMI SO_2). The mean anomaly profiles (black) and the monthly mean climatological tropopause altitude (horizontal black-dashed lines), plus the associated standard deviation of the individual-profile tropopause altitudes (shaded gray), are also indicated. For the Nabro after-eruption events (f and h) in addition the mean primary tropopause altitude (violet dashed line) and the mean secondary tropopause altitude (blue dashed line) are shown, together with the corresponding standard deviations (pink and cyan shaded). (For interpretation of the references to color in this figure legend, the reader is referred to the web version of this article.)
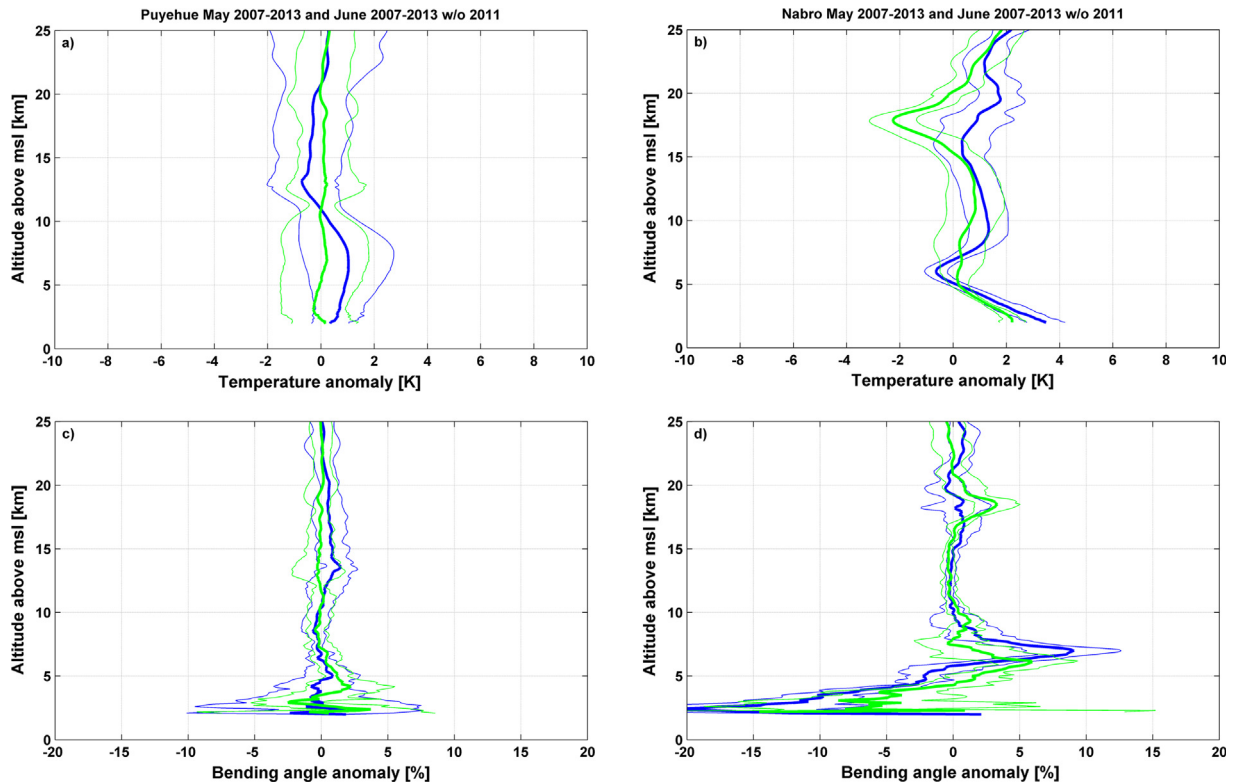
Fig. 3. Multiyear-averaged monthly mean temperature (top) and bending angle (bottom) anomaly profile, averaged over May 2007–2013 (heavy green) and June 2007–2013 without the month of eruption June 2011 (heavy blue), in the area of Puyehue (left) and Nabro (right). For indicating an estimated uncertainty range from inter-annual climate variability, also the standard deviation of the individual monthly mean anomaly profiles about the multiyear-average is depicted in all panels, as an envelope about the multiyear average profile, for both May (light green) and June (light blue). (For interpretation of the references to color in this figure legend, the reader is referred to the web version of this article.)

during these years, for the areas of Puyehue and Nabro. In the Puyehue region, monthly mean temperature anomalies in the UTLS stay within about ±1.5 K in both months. In the Nabro region, the monthly mean temperature anomaly above the tropical tropopause reaches colder values in May (about –2 K ± 1.5 K) than in June (about 1 K ± 1.5 K), due to higher convective activity.

In Fig. 4 we furthermore show the situation for the areas of Puyehue and Nabro in June 2010, one year before the eruptions when no volcanic clouds were present. We analyzed the meteorological conditions for both areas using MODIS data. We selected profiles in a deep-convective environment (green) and in a non-deep-convective environment (blue) (denoting here cloudy profiles with cloud top altitude lower than 300 hPa or clear sky). Fig. 4 shows that the June 2010 mean anomalies are similar to the climatological means. Temperature and bending angle anomalies are larger in the presence of deep convective clouds while they are smaller in the absence of deep convective clouds and do not differ that much from the climatology.

In the Nabro area it was very convective from 1 June to 11 June 2011 explaining why the temperature profiles before the eruption show clear cold anomalies (see Fig. 2e). Moreover, it is shown that in the Nabro area the tropospheric inversion at about 6 km altitude is also present in May and June monthly means (Fig. 3b) and in

June 2010 under normal conditions (no volcanic eruptions) (Fig. 4b).

Overall we find from Figs. 2–4 clear evidence that the mean anomaly profiles after volcanic eruptions show a significantly different structure than those under climatological conditions. For dynamical reasons it is extremely unlikely that the distinct spike-shaped mean anomaly signature in the RO profiles, which appears within days after the eruption date, would be the effect of smooth large-scale patterns of atmospheric variability modes.

Our estimates of background variability in the investigated regions, shown in Fig. 3, include also variability due the Quasi-Biennial Oscillation (QBO) and El Niño-Southern Oscillation (ENSO), which are the strongest background climate variability modes with potential influence. We specifically inspected therefore the potential effects of QBO and ENSO also for the time period around June 2011, based on an analysis of RO temperature time series in the tropical tropopause region by Randel and Wu (2015).

This analysis, which includes results with and without removal of QBO and ENSO signals, confirms that both QBO and ENSO as well as other remaining variability is not stronger than around 1 K from May 2011 to end of 2011 (Randel and Wu, 2015; Fig. 12 therein), which is within our estimated background variability of ±1.5 K.
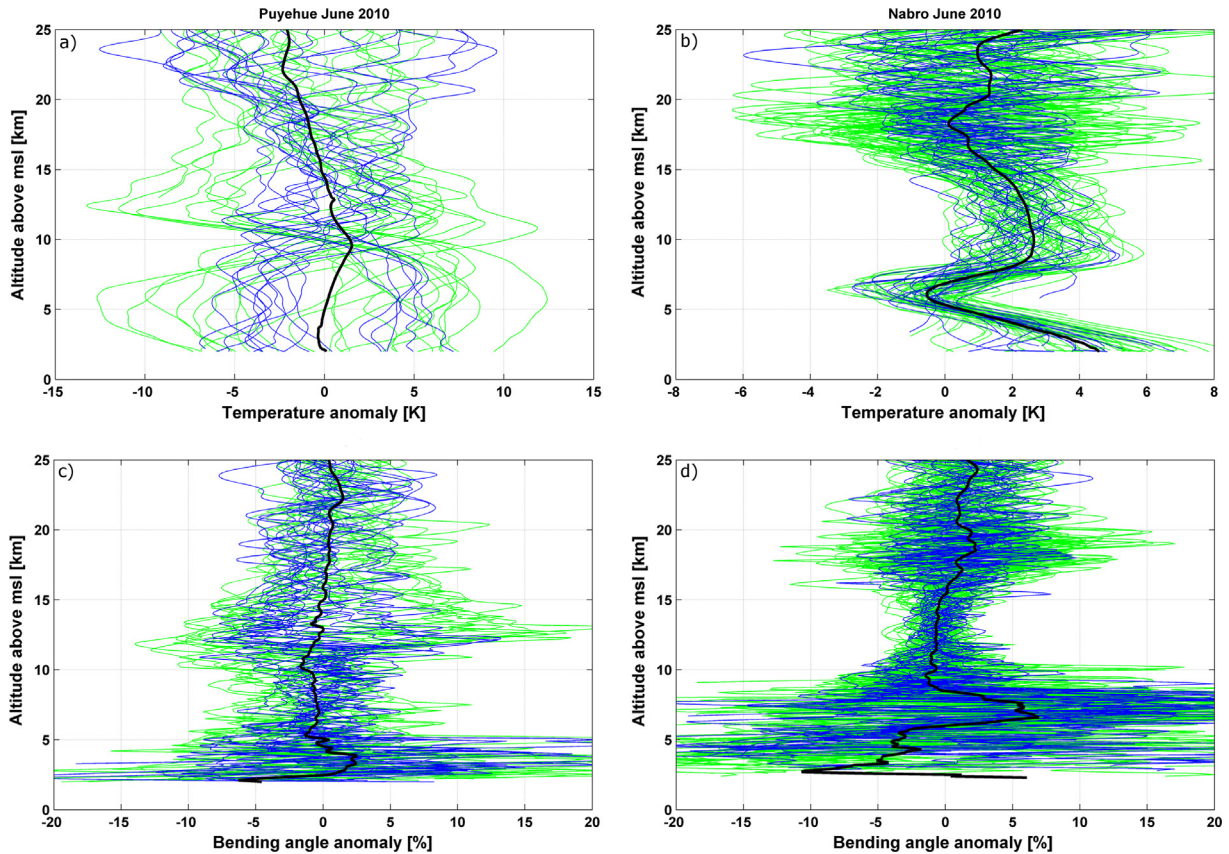
Fig. 4. Individual temperature anomaly profiles (top panels) and bending angle anomaly profiles (bottom panels) in deep-convective environment (green), in non-deep-convective environment (blue), and mean anomaly profile for the whole profile ensemble (black), shown for June 2010 in the area of Puyehue (a and c) and Nabro (b and d), respectively. (For interpretation of the references to color in this figure legend, the reader is referred to the web version of this article.)

Also a more general study of spatial and temporal ENSO characteristics by Scherllin-Pirscher et al. (2012) corroborates this finding by showing that the ENSO variability is within our estimated background variability.

Quantitatively we see a cooling of about 2 K in the mean after the Puyehue eruption (ash cloud) and a warming of about 4 K in the mean after the Nabro eruption (SO$_2$ cloud), which clearly are distinct signatures relative to the background variability of ±1.5 K.

5.3. Evolution of the anomaly signatures after the month of eruption

The further evolution of the atmospheric structure in the Puyehue area is presented in Fig. 5 until August 2011. It shows that the cooling after the volcanic eruption persisted for about two months into July 2011, whereas in August 2011 and subsequent months (not shown) the thermal structure had recovered and was back to normal climatological conditions (cf. Figs. 3a and 4a).

Fig. 6 shows the evolution of the atmospheric temperature structure for Nabro one month before the eruption (May 2011), during the month of the eruption (June 2011) and six months after the eruption (July to December 2011). The temperature anomaly profiles in Fig. 6 indicate that the stratospheric warming in the area of the volcano remained for several months in this case. In May the average temperature anomaly in the UTLS was about –1 K. In June before the eruption (green profiles) the average temperature anomaly reached about –2.5 K, but just after the eruption (red profiles) the trend became opposite with a temperature anomaly of about 4 K in the mean, and of up to 10 K for individual profiles. The positive stratospheric temperature anomaly in the Nabro area persisted until October 2011, decreasing in amplitude after August 2011, and then vanished.

Nabro injected about 1.5 Mt SO$_2$ into the stratosphere that caused an enhancement of stratospheric (hydrated sulfate) aerosol (Bourassa et al., 2012; Robock, 2013). Extended aerosol layers up to 20 km altitude were measured for several months after the eruption, for the first few weeks confined over North Africa and the monsoon region due to the monsoon anticyclonic vortex and then spread over the larger Northern Hemisphere, causing warming of the lower stratosphere (Bourassa et al., 2012). Although the dominant aerosol increase was north of the Nabro location (>20°N), results of Andersson et al. (2015, Fig. 4 therein) on aerosol load and radiative
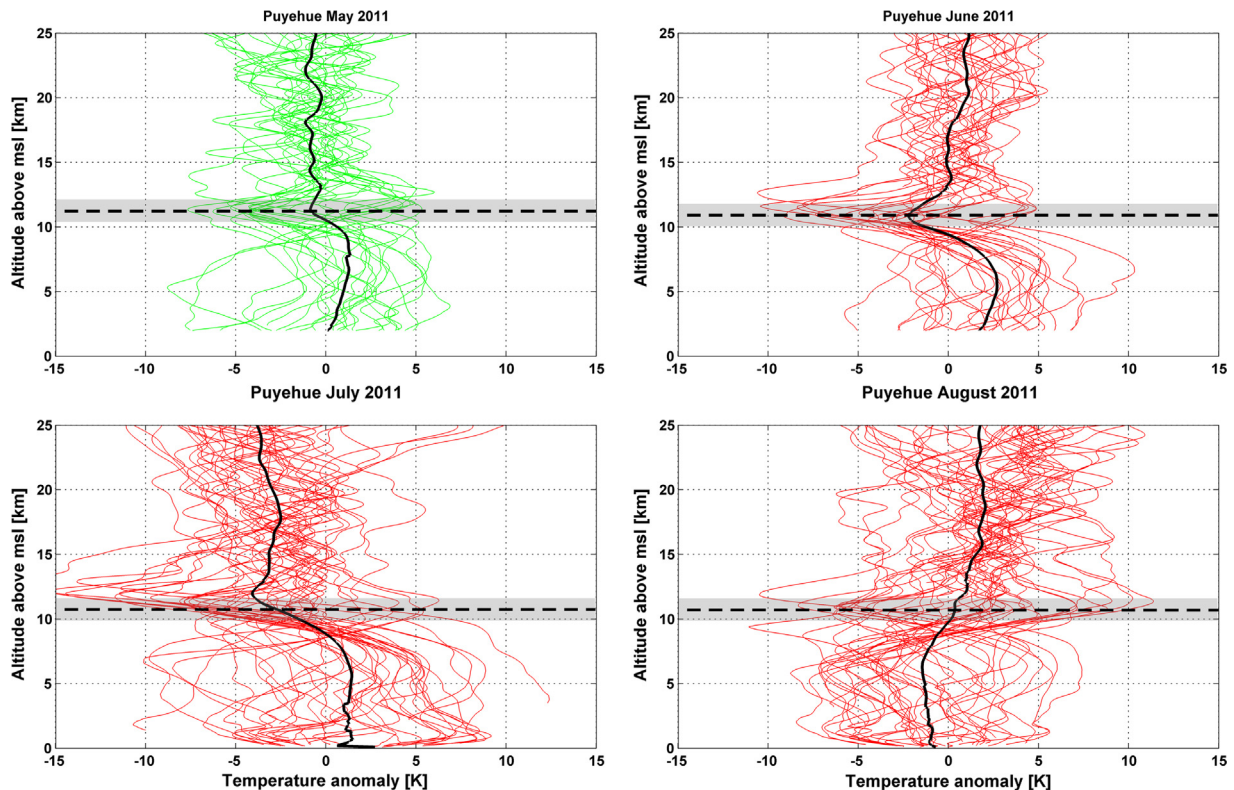
Fig. 5. Individual temperature anomaly profiles before the eruption (green) and after the eruption (red) with mean anomaly profile (black) in the area of the Puyehue volcano (10×10 degrees box in latitude and longitude), showing the evolution of the thermal structure from May 2011 to August 2011 (Puyehue eruption early June 2011). Climatological tropopause altitude for each month (black dashed line) with its standard deviation (shaded gray). (For interpretation of the references to color in this figure legend, the reader is referred to the web version of this article.)

forcing over 2008–2012 show the Nabro influence in the second half of 2011 also in the tropical latitude band (<20°N). This aerosol enhancement presumably explains the warming in the Nabro region over a few months after the eruption as seen in Fig. 6.

6. Conclusions

Cloud structure and cloud top height are key parameters for the monitoring of volcanic cloud movement and for characterizing eruptive processes and understanding the impact on short-term climate variability.

We introduced a technique that uses as a first step radiometric imaging observations in the thermal infrared (AIRS) and UV-visible (OMI) for identifying volcanic ash and SO_2 clouds and for discriminating against water clouds. In a second step we use geographically co-located profile observations from GNSS RO for detecting the cloud top altitude and for analyzing the thermodynamic influence of volcanic clouds. We demonstrated that the anomaly technique developed by Biondi et al. (2012, 2013) for detecting cloud tops of convective systems and tropical cyclones can also be used for detecting and monitoring volcanic cloud tops and cloud impacts on the thermal structure.

We showed the feasibility for the two largest eruptions (Puyehue 2011, Nabro 2011) in the RO data period since

the FORMSAT-3/COSMIC launch in 2006, where we could analyze about 1300 RO profiles for the two cases. We also found that the method works for smaller eruptions such as the Eyjafjöll eruption in Iceland in 2010 (Stohl et al., 2011). However, the number of cloud-collocated profiles was too small for a more detailed analysis, a situation that will drastically improve with the increased number of GNSS RO observations becoming available in future.

A different impact on the atmospheric thermal structure was found for the two study cases, volcanic ash clouds and SO_2 clouds. Our results revealed a cooling of about 2 K near the cloud top for ash clouds, confirming previous findings. In contrast, we found a clear warming signature from SO_2 (and hydrated sulfate) clouds after the eruption of Nabro, with mean amplitudes of about 4 K just after the eruption and persisting for a few months. Related to the climatological background variability of about ±1.5 K, including QBO and ENSO variability, these features clearly appear to be distinct volcanic signatures in the inspected $10° \times 10°$ regions around the volcanoes.

From this encouraging evidence we conclude that, due to their independence from weather conditions and due to their high vertical resolution, RO observations can contribute to improved detection and monitoring of volcanic clouds and to support warning systems. The high accuracy and vertical resolution of RO observations for detecting
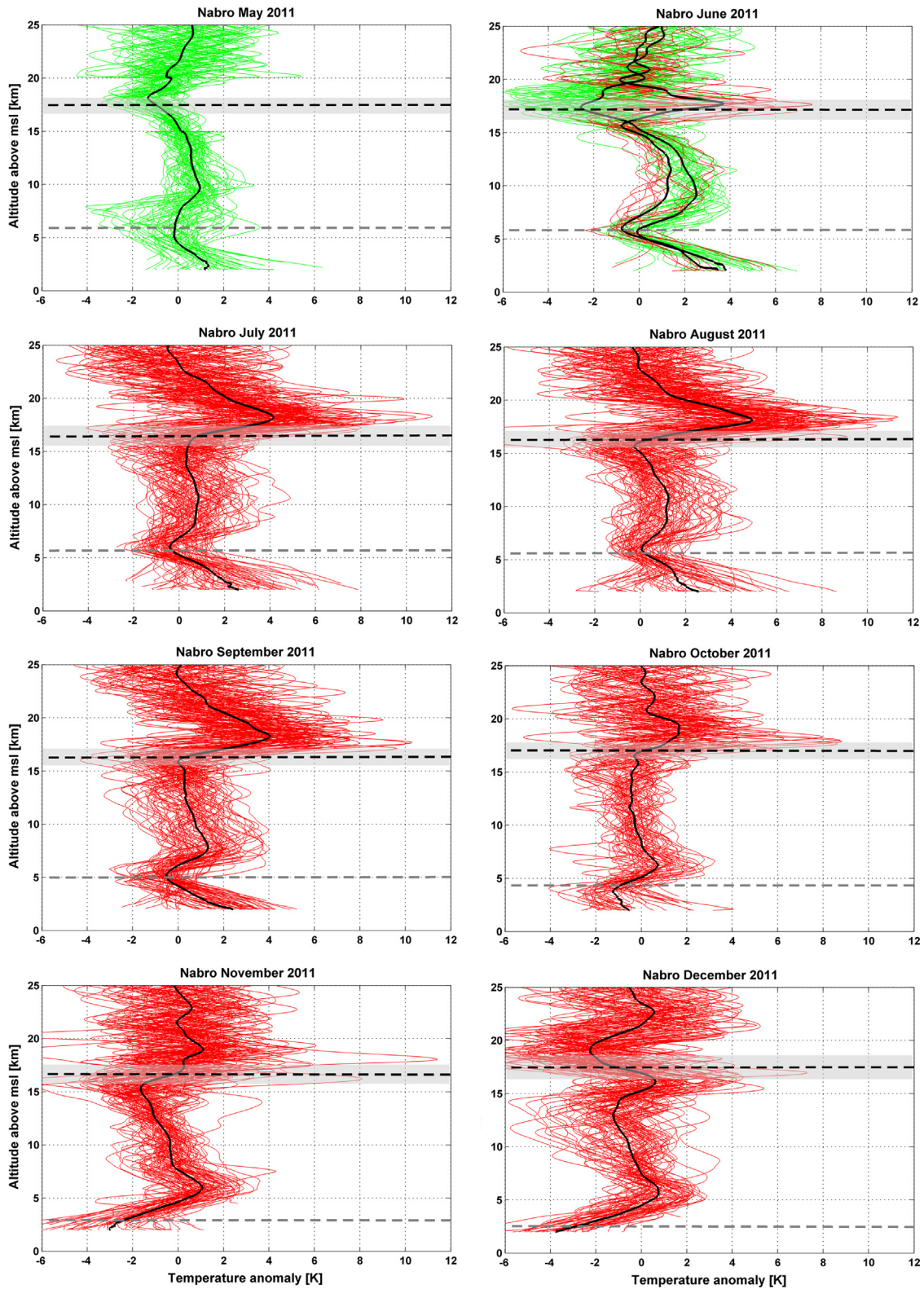
Fig. 6. Individual temperature anomaly profiles before the eruption (green) and after the eruption (red) with mean anomaly profile (black) in the area of the Nabro volcano (10 × 10 degrees box in latitude and longitude), showing the evolution of the thermal structure from May 2011 to December 2011 (Nabro eruption in June 2011). For June 2011 mean anomaly profiles are shown for pre-eruption and for post-eruption cases. Climatological tropopause altitude for each month (black dashed line) with its standard deviation (shaded gray). The average altitude of the tropospheric aerosol cloud from CALIOP measurements is indicated in each panel (gray dashed line). (For interpretation of the references to color in this figure legend, the reader is referred to the web version of this article.)

the tropopause with global coverage will also help to understand whether eruptions overshoot into the stratosphere and contribute to short-term climate variability.

Several new RO missions are planned for the near future, like the COSMIC-2 constellation and further RO receivers in the European MetOp and Chinese FY3 meteorological satellite series. These, together with a much higher number of GNSS signals from the U.S. GPS, the Russian GLONASS, the European Galileo system, and the Chinese Beidou system will provide RO profiles with unprecedented coverage in space and time for monitoring the thermal structure impacts of volcanic eruptions and their cloud dispersions at any stage.

Beyond the RO technique using the decimeter-wave GNSS signals, next-generation occultation techniques between Low Earth Orbit satellites are emerging that use centimeter- and millimeter-wave microwave signals (Kursinski et al., 2002, 2009; Kirchengast and Hoeg, 2004; Schweitzer et al., 2011a) and also micrometer-wave infrared laser signals (Kirchengast and Schweitzer, 2011; Schweitzer et al., 2011b; Proschek et al., 2011, 2014; Plach et al., 2015; Syndergaard and Kirchengast, 2016). These can simultaneously measure the thermodynamic structure, water and ice cloud structure, aerosol layering, atmospheric composition, and wind conditions and will therefore allow another drastic advancement of detecting and monitoring volcanic clouds by occultation methods in the future.

Acknowledgements

References

Alharbi, B.H., Maghrabi, A., Tapper, N., 2013. The March 2009 Dust Event in Saudi Arabia: precursor and supportive environment. Bull. Am. Meteorol. Soc. 94, 515–528. http://dx.doi.org/10.1175/BAMS-D-11-00118.1.

Andersson, S.M., Martinsson, B.G., Vernier, J.-P., Friberg, J., Brenninkmeijer, C.A.M., Hermann, M., van Velthoven, P.F.J., Zahn, A., 2015. Significant radiative impact of volcanic aerosol in the lowermost stratosphere. Nat. Commun. 6, 7692. http://dx.doi.org/10.1038/ncomms8692.

Anthes, R.A., Bernhardt, P.A., Chen, Y., Cucurull, L., Dymond, K.F., Ector, D., Healy, S., Ho, S.-P., Hunt, D., Kuo, Y.-H., Liu, H., Manning, K., McCormick, C., Meehan, T.K., Randel, W., Rocken, C., Schreiner, W.S., Sokolovskiy, S.V., Syndergaard, S., Thompson, D.C., Trenberth, K.E., Wee, T.K., Yen, N.L., Zeng, Z., 2008. The COSMIC/Formosat/3 mission: early results. Bull. Am. Meteorol. Soc. 89, 313–333. http://dx.doi.org/10.1175/BAMS-89-3-313.

Anthes, R.A., 2011. Exploring Earth's atmosphere with radio occultation: contributions to weather, climate and space weather. Atmos. Meas. Tech. 4, 1077–1103. http://dx.doi.org/10.5194/amt-4-1077-2011.

Aumann, H.H., Chahine, M.T., Gautier, C., Goldberg, M-D., Kalnay, E., McMillin, L.M., Revercomb, H., Rosenkranz, P.W., Smith, W.L., Staelin, D.H., Strow, L.L., Susskind, J., 2003. AIRS/AMSU/HSB on the Aqua mission: design, science objectives, data products, and processing systems. IEEE Trans. Geosci. Remote Sens. 41, 253–264. http://dx.doi.org/10.1109/TGRS.2002.808356.

Beyerle, G., Schmidt, T., Michalak, G., Heise, S., Wickert, J., Reigber, C., 2005. GPS radio occultation with GRACE: atmospheric profiling utilizing the zero difference technique. Geophys. Res. Lett. 32, L13806. http://dx.doi.org/10.1029/2005GL023109.

Bignami, C., Corradini, S., Merucci, L., de Michele, M., Raucoules, D., De Astis, G., Stramondo, S., Piedra, J., 2014. Multisensor satellite monitoring of the 2011, Puyehue-Cordon Caulle eruption. J. Sel. Top. Appl. Earth Observ. Remote Sens. 7, 2786–2796. http://dx.doi.org/10.1109/JSTARS.2014.2320638.

Biondi, R., Randel, W.J., Ho, S.-P., Neubert, T., Syndergaard, S., 2012. Thermal structure of convective clouds derived from GPS radio occultations. Atmos. Chem. Phys. 12, 5309–5318. http://dx.doi.org/10.5194/acp-12-5309-2012.

Biondi, R., Ho, S.-P., Randel, W.J., Neubert, T., Syndergaard, S., 2013. Tropical cyclone cloud-top height and vertical temperature structure detection using GPS radio occultation measurements. J. Geophys. Res. Atmos. 118, 5247–5259. http://dx.doi.org/10.1002/jgrd.50448.

Biondi, R., Steiner, A.K., Kirchengast, G., Rieckh, T., 2015. Characterization of thermal structure and conditions for overshooting of tropical and extratropical cyclones with GPS radio occultation. Atmos. Chem. Phys. 15, 5181–5193. http://dx.doi.org/10.5194/acp-15-5181-2015.

Biondi, R., Steiner, A., Kirchengast, G., Brenot, H., Rieckh, T., 2016. A novel technique including GPS radio occultation for detecting and monitoring volcanic clouds. Atmos. Chem. Phys. Discuss. http://dx.doi.org/10.5194/acp-2015-974.

Bourassa, A.E., Robock, A., Randel, W.J., Deshler, T., Rieger, L.A., Lloyd, N.D., Llewellyn, E.J., Degenstein, D.A., 2012. Large volcanic aerosol load in the stratosphere linked to asian monsoon transport. Science 337, 78–81. http://dx.doi.org/10.1126/science.1219371.

Bourassa, A.E., Robock, A., Randel, W.J., Deshler, T., Rieger, L.A., Lloyd, N.D., Llewellyn, E.J., Degenstein, D.A., 2013. Response to comment on "Large volcanic aerosol load in the stratosphere linked to asian monsoon transport". Science 339, 647. http://dx.doi.org/10.1126/science.1227961.

Brenot, H., Theys, N., Clarisse, L., van Geffen, J., van Gent, J., Van Roozendael, M., van der, A.R., Hurtmans, D., Coheur, P.-F., Clerbaux, C., Valks, P., Hedelt, P., Prata, F., Rasson, O., Sievers, K., Zehner, C., 2014. Support to Aviation Control Service (SACS): an online service for near-real-time satellite monitoring of volcanic plumes. Nat. Hazards Earth Syst. Sci. 14, 1099–1123. http://dx.doi.org/10.5194/nhess-14-1099-2014.

Cardinali, C., 2009. Monitoring the observation impact on the short-range forecast. Quar. J. Roy. Meteor. Soc. 135, 239–250. http://dx.doi.org/10.1002/qj.366.

Chang, F.-L., Minnis, P., Ayers, J.K., McGill, M.J., Palikonda, R., Spangenberg, D.A., Smith Jr., W.L., Yost, C.R., 2010. Evaluation of

satellite-based upper troposphere cloud top height retrievals in multilayer cloud conditions during TC4. J. Geophys. Res. 115, D00J05. http://dx.doi.org/10.1029/2009JD013305.

Clarisse, L., Hurtmans, D., Clerbaux, C., Hadji-Lazaro, J., Ngadi, Y., Coheur, P.-F., 2012. Retrieval of sulphur dioxide from the infrared atmospheric sounding interferometer (IASI). Atmos. Meas. Tech. 5, 581–594. http://dx.doi.org/10.5194/amt-5-581-2012.

Clarisse, L., Coheur, P.-F., Prata, F., Hadji-Lazaro, J., Hurtmans, D., Clerbaux, C., 2013. A unified approach to infrared aerosol remote sensing and type specification. Atmos. Chem. Phys. 13, 2195–2221. http://dx.doi.org/10.5194/acp-13-2195-2013.

Clarisse, L., Coheur, P.-F., Theys, N., Hurtmans, D., Clerbaux, C., 2014. The 2011 Nabro eruption, a SO_2 plume height analysis using IASI measurements. Atmos. Chem. Phys. 14, 3095–3111. http://dx.doi.org/10.5194/acp-14-3095-2014.

Dubuisson, P., Frouin, R., Dessailly, D., Duforet, L., Leon, J., Voss, K., Antoine, D., 2009. Estimating the altitude of aerosol plumes over the ocean from reflectance ratio measurements in the O_2 A-band. Remote Sens. Environ. 113, 1899–1911. http://dx.doi.org/10.1016/j.rse.2009.04.018.

Foelsche, U., Scherllin-Pirscher, B., Ladstädter, F., Steiner, A.K., Kirchengast, G., 2011. Refractivity and temperature climate records from multiple radio occultation satellites consistent within 0.05%. Atmos. Meas. Tech. 4, 2007–2018. http://dx.doi.org/10.5194/amt-4-2007-2011.

Frey, R.A., Baum, B.A., Menzel, W.P., Ackerman, S.A., Moeller, C.C., Spinhirne, J.D., 1999. A comparison of cloud top heights computed from airborne lidar and MAS radiance data using CO_2 slicing. J. Geophys. Res. 104, 24547–24555. http://dx.doi.org/10.1029/1999JD900796.

Fromm, M., Nedoluha, G., Charvat, Z., 2013. Comment on "Large volcanic aerosol load in the stratosphere linked to asian monsoon transport". Science 339. http://dx.doi.org/10.1126/science.1228605.

Fromm, M., Kablick III, G., Nedoluha, G., Carboni, E., Grainger, R., Campbell, J., Lewis, J., 2014. Correcting the record of volcanic stratospheric aerosol impact: Nabro and Sarychev Peak. J. Geophys. Res. Atmos. 119, 10343–10364. http://dx.doi.org/10.1002/2014JD021507.

Genkova, I., Seiz, G., Zuidema, P., Zhao, G., Di Girolamo, L., 2007. Cloud top height comparisons from ASTER, MISR, and MODIS for trade wind cumuli. Remote Sens. Environ. 107, 211–222. http://dx.doi.org/10.1016/j.rse.2006.07.021.

Global Volcanism Program, 2013. Report on Puyehue-Cordon Caulle (Chile), In: Wunderman, R (ed.), Bulletin of the Global Volcanism Network, 38:9, Smithsonian Institution. doi: http://dx.doi.org/10.5479/si.GVP.BGVN201309-357150.

Global Volcanism Program, 2014. Report on Nabro (Eritrea). In: Wunderman, R (ed.), Bulletin of the Global Volcanism Network, 39:5, Smithsonian Institution. doi: http://dx.doi.org/10.5479/si.GVP.BGVN201405-221101.

Gorbunov, M.E., Benzon, H.-H., Jensen, A.S., Lohmann, M.S., Nielsen, A.S., 2004. Comparative analysis of radio occultation processing approaches based on Fourier integral operators. Radio Sci. 39, RS6004. http://dx.doi.org/10.1029/2003RS002916.

Hajj, G.A., Ao, C.O., Iijima, B.A., Kuang, D., Kursinski, E.R., Mannucci, A.J., Meehan, T.K., Romans, L.J., de la Torre Juarez, M., Yunck, T.P., 2004. CHAMP and SAC-C atmospheric occultation results and intercomparisons. J. Geophys. Res. 109, D06109. http://dx.doi.org/10.1029/2003JD003909.

Harris, D.M., Rose, W.I., Roe, R., Thompson, M.R., 1981. Radar observations of ash eruptions. US Geol. Surv. Pap. 1250, 323–333.

Harris, D.M., Rose, W.I.J., 1983. Estimating particle size, concentrations, and total mass of ash in volcanic clouds using weather data. J. Geophys. Res. 88, 10969–10983. http://dx.doi.org/10.1029/JC088iC15p10969.

Ho, S.-P., Hunt, D., Steiner, A.K., Mannucci, A.J., Kirchengast, G., Gleisner, H., Heise, S., von Engeln, A., Marquardt, C., Sokolovskiy, S., Schreiner, W., Scherllin-Pirscher, B., Ao, C., Wickert, J., Syndergaard, S., Lauritsen, K., Leroy, S., Kursinski, E.R., Kuo, Y.-H., Foelsche, U., Schmidt, T., Gorbunov, M., 2012. Reproducibility of GPS radio occultation data for climate monitoring: profile-to-profile inter-comparison of CHAMP climate records 2002 to 2008 from six data centers. J. Geophys. Res. 117, D18111. http://dx.doi.org/10.1029/2012JD017665.

Holasek, R.E., Self, S., 1995. GOES weather satellite observations and measurements of the May 18, 1980, Mount St. Helens eruption. J. Geophys. Res. 100, 8469–8487. http://dx.doi.org/10.1029/94JB03137.

Huang, C.-Y., Kuo, Y.-H., Chen, S.-H., Vandenberghe, F., 2005. Improvements in Typhoon forecasts with assimilated GPS occultation refractivity. Wea. Forecasting 20, 931–953. http://dx.doi.org/10.1175/WAF874.1.

IFALPA, 2011. The Global Voice of Pilots: Flight operations in the presence of volcanic contamination, 12POS01, 27 July 2011, <http://www.ifalpa.org/downloads/Level1/IFALPA%20Statements/Aircraft%20Design%20&%20Operation/12POS01%20-%20Operations%20in%20the%20presence%20of%20volcanic%20contamination.pdf>. (accessed on 12 February 2017).

IUGG, 2010. Volcanological and meteorological support for volcanic ash monitoring, Statement adopted by the IUGG Bureau on 28 May 2010, Available at <http://www.iugg.org/resolutions/IUGG_Statement_VMSVolcAshMonit.pdf>.

King, M.D., Platnick, S., Menzel, W.P., Ackerman, S.A., Hubanks, P.A., 2013. Spatial and temporal distribution of clouds observed by MODIS onboard the terra and aqua satellites. IEEE Trans. Geosci. Remote Sens. 51, 3826–3852. http://dx.doi.org/10.1109/TGRS.2012.2227333.

Kirchengast, G., Hoeg, P., 2004. The ACE+ mission: an atmosphere and climate explorer based on GPS, GALILEO, and LEO-LEO radio occultation. In: Kirchengast, G., Foelsche, U., Steiner, A.K. (Eds.), Occultations for Probing Atmosphere and Climate. Springer Verlag, Berlin, pp. 201–220.

Kirchengast, G., Schweitzer, S., 2011. Climate benchmark profiling of greenhouse gases and thermodynamic structure and wind from space. Geophys. Res. Lett. 38, L13701. http://dx.doi.org/10.1029/2011GL047617.

Kursinski, E.R., Hajj, G.A., Schofield, J.T., Linfield, R.P., Hardy, K.R., 1997. Observing Earth's atmosphere with radio occultation measurements using the Global Positioning System. J. Geophys. Res. 102, 23429–23465. http://dx.doi.org/10.1029/97JD01569.

Kursinski, E.R., Syndergaard, S., Flittner, D., Feng, D., Hajj, G., Herman, B., Ward, D., Yunck, T., 2002. A microwave occultation observing system optimized to characterize atmospheric water, temperature, and geopotential via absorption. J. Atmos. Oceanic Technol. 19, 1897–1914. http://dx.doi.org/10.1175/1520-0426(2002) 019.

Kursinski, E.R., Ward, D., Otarola, A., Frehlich, K., Groppi, C., Albanna, S., Shein, M., Bertiger, W., Pickett, H., Ross, M., 2009. The Active Temperature, Ozone and Moisture Microwave Spectrometer (ATOMMS). In: Steiner, A.K., Pirscher, B., Foelsche, U., Kirchengast, G. (Eds.), New Horizons in Occultation Research. Springer Verlag, Berlin, pp. 295–313. http://dx.doi.org/10.1007/978-3-642-00321-9_24.

Ladstädter, F., Steiner, A.K., Schwärz, M., Kirchengast, G., 2015. Climate intercomparison of GPS radio occultation, RS90/92 radiosondes and GRUAN from 2002 to 2013. Atmos. Meas. Tech. 8, 1819–1834. http://dx.doi.org/10.5194/amt-8-1819-2015.

LeGrande, A.N., Tsigaridis, K., Bauer, S.E., 2016. Role of atmospheric chemistry in the climate impacts of stratospheric volcanic injections. Nat. Geosci. 9, 652–655. http://dx.doi.org/10.1038/ngeo2771.

Levelt, P.F., Hilsenrath, E., Leppelmeier, G.W., van den Oord, G.H.J., Bhartia, P.K., Tamminen, J., de Haan, J.F., Veefkind, J.P., 2006. Science objectives of the ozone monitoring instrument. IEEE Trans. Geosci. Remote Sens. 44, 1199–1208. http://dx.doi.org/10.1109/TGRS.2006.872336.

Luntama, J.-P., Kirchengast, G., Borsche, M., Foelsche, U., Steiner, A., Healy, S., von Engeln, A., O'Clerigh, E., Marquardt, C., 2008. Prospects of the EPS GRAS mission for operational atmospheric applications. Bull. Am. Meteorol. Soc. 89, 1863–1875. http://dx.doi.org/10.1175/2008BAMS2399.1.

Mackie, S., Cashman, K., Ricketts, H., Rust, A., Watson, M., 2016. Volcanic Ash: Hazard Observation. Elsevier, Amsterdam, ISBN 9780081004050.

Matson, M., 1984. The 1982 El Chichón Volcano eruptions – A satellite perspective. J. Volcanol. Geoth. Res. 23, 1–10. http://dx.doi.org/10.1016/0377-0273(84)90054-4.

McCormick, M.P., Thomason, L.W., Trepte, C.R., 1995. Atmospheric effects of the Mt Pinatubo eruption. Nature 373, 399–404. http://dx.doi.org/10.1038/373399a0.

Mehta, S.K., Fujiwara, M., Tsuda, T., Vernier, J.-P., 2015. Effect of recent minor volcanic eruptions on temperatures in the upper troposphere and lower stratosphere. J. Atmos. Solar-Terr. Phys. 129, 99–110. http://dx.doi.org/10.1016/j.jastp.2015.04.009.

Melbourne, W.G., Davis, E.S., Duncan, C.B., Hajj, G.A., Hardy, K.R., Kursinski, E.R., Meehan, T.K., Young, L.E., Yunck, T.P., 1994. The application of spaceborne GPS to atmospheric limb sounding and global change monitoring, JPL Publication 94-18, Jet Propulsion Lab, Pasadena, CA.

Okazaki, I., Heki, K., 2012. Atmospheric temperature changes by volcanic eruptions: GPS radio occultation observations in the 2010 icelandic and 2011 chilean cases. J. Volcanol. Geoth. Res. 245–246, 123–127. http://dx.doi.org/10.1016/j.jvolgeores.2012.08.018.

Plach, A., Proschek, V., Kirchengast, G., 2015. Profiling wind and greenhouse gases by infrared-laser occultation: results from end-to-end simulations in windy air. Atmos. Meas. Tech. 8, 2813–2825. http://dx.doi.org/10.5194/amt-8-2813-2015.

Pósfai, M., Duncan, A., Tompa, E., Freney, E., Bruintjes, R., Buseck, P. R., 2012. Interactions of mineral dust with pollution and clouds: an individual-particle TEM study of atmospheric aerosol from Saudi Arabia. Atmos. Res. 122, 347–361. http://dx.doi.org/10.1016/j.atmosres.2012.12.001.

Poulsen, C.A., Siddans, R., Thomas, G.E., Sayer, A.M., Grainger, R.G., Campmany, E., Dean, S.M., Arnold, C., Watts, P.D., 2012. Cloud retrievals from satellite data using optimal estimation: evaluation and application to ATSR. Atmos. Meas. Tech. 5, 1889–1910. http://dx.doi.org/10.5194/amt-5-1889-2012.

Prata, A.J., 2008. Satellite detection of hazardous volcanic clouds and the risk to global air traffic. Nat. Hazards 51, 303–324. http://dx.doi.org/10.1007/s11069-008-9273-z.

Prata, A.J., Dezitter, F., Davies, I., Weber, K., Birnfeld, M., Moriano, D., Bernardo, C., Vogel, A., Prata, G.S., Mather, T.A., Thomas, H.E., Cammas, J., Weber, M., 2016. Artificial cloud test confirms volcanic ash detection using infrared spectral imaging. Sci. Rep. 6, 25620.

Proschek, V., Kirchengast, G., Schweitzer, S., 2011. Greenhouse gas profiling by infrared-laser and microwave occultation: retrieval algorithm and demonstration results from end-to-end simulations. Atmos. Meas. Tech. 4, 2035–2058. http://dx.doi.org/10.5194/amt-4-2035-2011.

Proschek, V., Kirchengast, G., Emde, C., Schweitzer, S., 2014. Greenhouse gas profiling by infrared-laser and microwave occultation in cloudy air: results from end-to-end simulations. J. Geophys. Res. Atmos. 119, 12372–12390. http://dx.doi.org/10.1002/2014JD021938.

Raga, G.B., Baumgardner, D., Ulke, A.G., Torres Brizuela, M., Kucienska, B., 2013. The environmental impact of the Puyehue–Cordon Caulle 2011 volcanic eruption on Buenos Aires. Nat. Hazards Earth Syst. Sci. 13, 2319–2330. http://dx.doi.org/10.5194/nhess-13-2319-2013.

Randel, W.J., Wu, F., 2015. Variability of zonal mean tropical temperatures derived from a decade of GPS radio occultation data. J. Atmos. Sci. 72, 1261–1275. http://dx.doi.org/10.1175/JAS-D-14-0216.1.

Rieckh, T., Scherllin-Pirscher, B., Ladstädter, F., Foelsche, U., 2014. Characteristics of tropopause parameters as observed with GPS radio occultation. Atmos. Meas. Tech. 7, 3947–3958. http://dx.doi.org/10.5194/amt-7-3947-2014.

Robock, A., 2000. Volcanic eruptions and climate. Rev. Geophys. 38, 191–219. http://dx.doi.org/10.1029/1998RG000054.

Robock, A., 2013. The latest on volcanic eruptions and climate. Eos 94, 305–312. http://dx.doi.org/10.1002/2013EO350001.

Sawada, Y., 2004. Eruption cloud echo measured with C-band weather radar. In: Proceedings of the 2nd International Conference on Volcanic Ash and Aviation Safety, Alexandria, Virginia USA, 21–24 June, 2004.

Sawamura, P., Vernier, J.P., Barnes, J.E., Berkoff, T.A., Welton, E.J., Alados-Arboledas, L., Navas-Guzmán, F., Pappalardo, G., Mona, L., Madonna, F., Lange, D., Sicard, M., Godin-Beekmann, S., Payen, G., Wang, Z., Hu, S., Tripathi, S.N., Cordoba-Jabonero, C., Hoff, R.M., 2012. Stratospheric AOD after the 2011 eruption of Nabro volcano measured by lidars over the Northern Hemisphere. Environ. Res. Lett. 7, 034013. http://dx.doi.org/10.1088/1748-9326/7/3/034013.

Scherllin-Pirscher, B., Deser, C., Ho, S.-P., Chou, C., Randel, W., Kuo, X.-H., 2012. The vertical and spatial structure of ENSO in the upper troposphere and lower stratosphere from GPS radio occultation measurements. Geophys. Res. Lett. 39, L20801. http://dx.doi.org/10.1029/2012GL053071.

Scherllin-Pirscher, B., Steiner, A.K., Kirchengast, G., Kuo, Y.-H., Foelsche, U., 2011a. Empirical analysis and modeling of errors of atmospheric profiles from GPS radio occultation. Atmos. Meas. Tech. 4, 1875–1890. http://dx.doi.org/10.5194/amt-4-1875-2011.

Scherllin-Pirscher, B., Steiner, A.K., Kirchengast, G., Kuo, Y.-H., Foelsche, U., 2011b. Quantifying uncertainty in climatological fields from GPS radio occultation: an empirical-analytical error model. Atmos. Meas. Tech. 4, 2019–2034. http://dx.doi.org/10.5194/amt-4-2019-2011.

Scherllin-Pirscher, B., Steiner, A.K., Kirchengast, G., Schwärz, M., Leroy, S.S., 2017. The power of vertical geolocation of atmospheric profiles from GNSS radio occultation. J. Geophys. Res. Atmos. 122. http://dx.doi.org/10.1002/2016JD025902.

Smith, E., Weintraub, S., 1953. The constants in the equation for atmospheric refractive index at radio frequencies. Proc. IRE 41, 1035–1037.

Schweitzer, S., Kirchengast, G., Schwaerz, M., Fritzer, J., Gorbunov, M. E., 2011a. Thermodynamic state retrieval from microwave occultation data and performance analysis based on end-to-end simulations. J. Geophys. Res. 116, D10301. http://dx.doi.org/10.1029/2010JD014850.

Schweitzer, S., Kirchengast, G., Proschek, V., 2011b. Atmospheric influences on infrared-laser signals used for occultation measurements between Low Earth Orbit satellites. Atmos. Meas. Tech. 4, 2273–2292. http://dx.doi.org/10.5194/amt-4-2273-2011.

Schwärz, M., Kirchengast, G., Scherllin-Pirscher, B., Schwarz, J., Ladstädter, F., Angerer, B., 2016. Multi-mission validation by satellite radio occultation extension project—Final report, Tech. Rep. for ESA-ESRIN 01/2016, Wegener Center, Univ. of Graz, Austria, 164p.

Sparks, R.S.J., Bursik, M.I., Carey, S.N., Gilbert, J.S., Glaze, L.S., Sigurdsson, H., Woods, A.W., 1997. Volcanic Plumes. J. Wiley and Sons, Chichester, UK, p. 574.

Steiner, A.K., Hunt, D., Ho, S.-P., Kirchengast, G., Mannucci, A.J., Scherllin-Pirscher, B., Gleisner, H., von Engeln, A., Schmidt, T., Ao, C., Leroy, S.S., Kursinski, E.R., Foelsche, U., Gorbunov, M., Heise, S., Kuo, Y.-H., Lauritsen, K.B., Marquardt, C., Rocken, C., Schreiner, W., Sokolovskiy, S., Syndergaard, S., Wickert, J., 2013. Quantification of structural uncertainty in climate data records from GPS radio occultation. Atmos. Chem. Phys. 13, 1469–1484. http://dx.doi.org/10.5194/acp-13-1469-2013.

Steiner, A.K., Lackner, B.C., Ladstädter, F., Scherllin-Pirscher, B., Foelsche, U., Kirchengast, G., 2011. GPS radio occultation for climate monitoring and change detection. Radio Sci. 46, RS0D24. http://dx.doi.org/10.1029/2010RS004614.

Stohl, A., Prata, A.J., Eckhardt, S., Clarisse, L., Durant, A., Henne, S., Kristiansen, N.I., Minikin, A., Schumann, U., Seibert, P., Stebel, K., Thomas, H.E., Thorsteinsson, T., Tørseth, K., Weinzierl, B., 2011. Determination of time- and height-resolved volcanic ash emission and their use for quantitative ash dispersion modeling: the 2010 Eyjafjallajökull eruption. Atmos. Chem. Phys. 11, 4333–4351. http://dx.doi.org/10.5194/acp-11-4333-2011.

Syndergaard, S., Kirchengast, G., 2016. An Abel transform for deriving line-of-sight wind profiles from LEO-LEO infrared laser occultation measurements. J. Geophys. Res. Atmos. 121. http://dx.doi.org/10.1002/2015JD023535.

Textor, C., Graf, H.-F., Longo, A., Neri, A., Esposti Ongaro, T., Papale, P., Timmreck, C., Ernst, G.G.J., 2005. Numerical simulation of explosive volcanic eruptions from the conduit flow to global atmospheric scales. Ann. Geophys. 48, 817–842. http://dx.doi.org/10.4401/ag-3237.

Theys, N., Campion, R., Clarisse, L., Brenot, H., van Gent, J., Dils, B., Corradini, S., Merucci, L., Coheur, P.-F., Van Roozendael, M., Hurtmans, D., Clerbaux, C., Tait, S., Ferrucci, F., 2013. Volcanic SO_2 fluxes derived from satellite data: a survey using OMI, GOME-2, IASI and MODIS. Atmos. Chem. Phys. 13, 5945–5968. http://dx.doi.org/10.5194/acp-13-5945-2013.

Timmreck, C., Graf, H.-F., Steil, B., 2013. Aerosol Chemistry Interactions After the Mt. In: Robock, A., Oppenheimer, C. (Eds.), Pinatubo Eruption, Volcanism and the Earth's Atmosphere, American Geophysical Union, Washington, D.C. doi: http://dx.doi.org/10.1029/139GM13.

Tupper, A., Carn, S., Davey, J., Kamada, Y., Potts, R., Prata, F., Tokuno, M., 2004. An evaluation of volcanic cloud detection techniques during recent significant eruptions in the western "Ring of Fire". Remote Sens. Environ. 91, 27–46. http://dx.doi.org/10.1016/j.rse.2004.02.004.

Vernier, J.-P., Fairlie, T.D., Murray, J.J., Tupper, A., Trepte, C., Winker, D., Pelon, J., Garnier, A., Jumelet, J., Pavolonis, M., Omar, A.H., Powell, K.A., 2013a. An advanced system to monitor the 3d structure of diffuse volcanic ash clouds. J. Appl. Meteor. Climatol. 52, 2125–2138. http://dx.doi.org/10.1175/JAMC-D-12-0279.1.

Vernier, J.-P., Thomason, L.W., Fairlie, T.D., Minnis, P., Palikonda, R., Bedka, K.M., 2013b. Comment on "Large volcanic aerosol load in the stratosphere linked to asian monsoon transport". Science 339. http://dx.doi.org/10.1126/science.1227817.

Virtanen, T.H., Kolmonen, P., Rodriguez, E., Sogacheva, L., Sundström, A.-M., de Leeuw, G., 2014. Ash plume top height estimation using AATSR. Atm. Meas. Tech. 7, 2437–2456. http://dx.doi.org/10.5194/amt-7-2437-2014.

Wang, K.-Y., Lin, S.-C., Lee, L.-C., 2009. Immediate impact of the Mt Chaiten eruption on atmosphere from FORMOSAT-3/COSMIC constellation. Geophys. Res. Lett. 36, L03808. http://dx.doi.org/10.1029/2008GL036802.

Wickert, J., Christoph, R., Beyerle, G., König, R., Marquardt, C., Schmidt, T., Grunwaldt, L., Galas, R., Meehan, T.K., Melbourne, W. G., Hocke, K., 2001. Atmosphere sounding by GPS radio occultation: first results from CHAMP. Geophys. Res. Lett. 28, 3263–3266. http://dx.doi.org/10.1029/2001GL013117.

Wickert, J., Schmidt, T., Michalak, G., Heise, S., Arras, C., Beyerle, G., Falck, C., König, R., Pingel, D., Rothacher, M., 2009. GPS radio occultation with CHAMP, GRACE-A, SAC-C, TerraSAR-X, and FORMOSAT-3/COSMIC: Brief review of results from GFZ. In: Steiner, A.K., Pirscher, B., Foelsche, U., Kirchengast, G. (Eds.) New Horizons in Occultation Research: Studies in Atmosphere and Climate, Springer, Berlin Heidelberg, pp. 3–15. doi:http://dx.doi.org/10.1007/978-3-642-00321-9_1.

Winker, D.M., Vaughan, M.A., Omar, A., Hu, Y., Powell, K.A., Liu, Z., Hunt, W.H., Young, S.A., 2009. Overview of the CALIPSO mission and CALIOP data processing algorithms. J. Atmos. Oceanic Technol. 26, 2310–2323. http://dx.doi.org/10.1175/2009JTECHA1281.1.

Woods, A.W., 1988. The fluid dynamics and thermodynamics of eruption columns. Bull. Volcanol. 50, 169–193. http://dx.doi.org/10.1007/BF01079681.

Woods, A.W., Holasek, R.E., Self, S., 1995. Wind-driven dispersal of volcanic ash plumes and its control on the thermal structure of the plume-top. Bull. Volcanol. 57, 283–292. http://dx.doi.org/10.1007/BF00301288.

Yang, K., Krotkov, N.A., Krueger, A.J., Carn, S.A., Bhartia, P.K., Levelt, P.F., 2007. Retrieval of large volcanic SO_2 columns from the Aura Ozone Monitoring Instrument (OMI): comparison and limitations. J. Geophys. Res. 112, D24S43. http://dx.doi.org/10.1029/2007JD008825.

Zakšek, K., Hort, M., Zaletelj, J., Langmann, B., 2013. Monitoring volcanic ash cloud top height through simultaneous retrieval of optical data from polar orbiting and geostationary satellites. Atmos. Chem. Phys. 13, 2589–2606. http://dx.doi.org/10.5194/acp-13-2589-2013.

Zehner, C. (ed.), 2010. Monitoring volcanic ash from space, Proceedings of the ESA-EUMETSAT workshop on the 14 April to 23 May 2010 eruption at the Eyjafjöll volcano, South Iceland. Frascati, Italy, 26–27 May 2010, ESA-Publication STM-280. doi:http://dx.doi.org/10.5270/atmch-10-01.